Advancing Sensorless Freehand 3D Ultrasound Reconstruction with a Novel Coupling Pad

Ling Dai[1,2], Kaitao Zhao[3], Zhongyu Li[2], Jihua Zhu[2⋆], and Libin Liang[1,4⋆]

[1] Key Laboratory of Biomedical Information Engineering of Ministry of Education, Department of Biomedical Engineering, School of Life Science and Technology, Xi'an Jiaotong University, Xi'an, Shaanxi, China
lianglibin@xjtu.edu.cn
[2] School of Software Engineering, Xi'an Jiaotong University, Xi'an, Shaanxi, China
[3] Shaanxi Second Provincial People's Hospital
[4] Research Institute of Xi'an Jiaotong University, Zhejiang, China

Abstract. Sensorless freehand 3D ultrasound (US) reconstruction poses a significant challenge, yet it holds considerable importance in improving the accessibility of 3D US applications in clinics. Current mainstream solutions, relying on inertial measurement units or deep learning, encounter issues like cumulative drift. To overcome these limitations, we present a novel sensorless 3D US solution with two key contributions. Firstly, we develop a novel coupling pad for 3D US, which can be seamlessly integrated into the conventional 2D US scanning process. This pad, featuring 3 N-shaped lines, provides 3D spatial information without relying on external tracking devices. Secondly, we introduce a coarse-to-fine optimization method for calculating poses of sequential 2D US images. The optimization begins with a rough estimation of poses and undergoes refinement using a distance-topology discrepancy reduction strategy. The proposed method is validated by both simulation and practical phantom studies, demonstrating its superior performance compared to state-of-the-art methods and good accuracy in 3D US reconstruction.

Keywords: Sensorless · Freehand 3D ultrasound · Coupling pad · Optimization.

1 Introduction

Ultrasound (US) imaging is a critical tool in image-guided interventions, providing guidance for surgical devices and real-time monitoring of tissues. It offers advantages such as low cost, safety, and portability. In recent years, 3D US imaging has attracted considerable attention for its improved intuitive visuals and richer contextual details. The generation of 3D US images can be achieved through several methods, such as dedicated 3D probes, mechanical scanning, or freehand scanning paired with external tracking devices [5,14]. Nonetheless, the cost associated with 3D US probes and the complexities introduced by tracking or mechanical devices limit their broad adoption in clinical practices.

⋆ Corresponding authors.

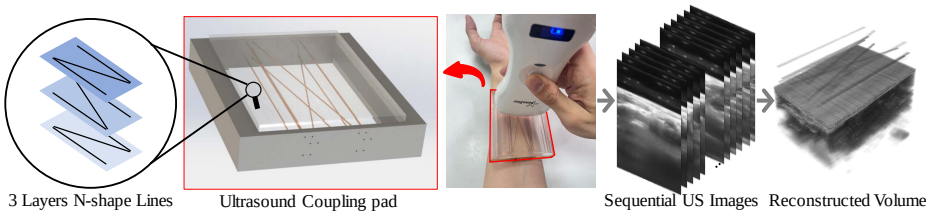

Fig. 1. The proposed coupling pad for sensorless 3D US reconstruction.

Consequently, there is a growing interest in developing lightweight and cost-effective 3D US solutions tailored for image-guided interventions. A prevalent approach is combining Inertial Measurement Units (IMUs) with conventional 2D US probes. For instance, Morgan et al. [13] attached a low-cost IMU to a US probe on a custom single-axis rotating fixture, enabling 3D US generation from 2D images. More advanced studies focused on integrating deep learning techniques to enhance the IMU-based solutions, such as the application of convolutional neural network (CNN) [16], the deep motion network (MoNet) [7], and the hybrid transformer encoder [15]. Additionally, Luo et al. [8] also proposed a multi-IMU-based solution for freehand 3D US reconstruction, aiming to reduce noise impact from individual IMU data.

Further efforts are being made to develop sensorless 3D US solutions, aiming to eliminate the need for physical tracking devices on US probes. These sensorless solutions are crucial in reducing the costs of 3D ultrasound and enhancing its accessibility in clinics, especially for underdeveloped countries. Early research in this area explored speckle decorrelation techniques to estimate relative motion between neighboring US images by analyzing speckle patterns [1,18]. Recently, numerous deep learning-based methods have emerged. Prevost et al. [17] were pioneers in using CNN for estimating transformations between two adjacent 2D US images. Likewise, several other neural networks were developed to improve estimation accuracy, including a pyramid warping network [19], a deep network with a Siamese architecture [2], and a hybrid network combining ResNet and FlowNetS [11]. Recognizing that a sequence of 2D US frames offers a more general representation of the US probe's motion, Recurrent Neural Networks (RNNs) were introduced in several studies [12,6]. Guo et al. also used sequential US images, and advanced trajectory estimation of US probe with the Deep Contextual Learning Network (DCL-Net) [3] and Deep Contextual-Contrastive Network [4]. Additionally, Luo et al. [9,10] designed an online learning framework (OLF) that improves reconstruction performance by utilizing consistency constraints and shape priors.

Despite these advancements, deep learning-based methods still face challenges, such as the difficult estimation of elevational displacement and significant cumulative drift. Moreover, the effectiveness of deep learning techniques heavily relies on the training images which vary across different US machines, thereby limiting their application in clinical settings. Prior sensorless 3D US studies were

mainly based on analysis of 2D US images, lacking distinct patterns essential for accurate image localization. In this paper, we developed a novel method for sensorless 3D US reconstruction, overcoming the above limitation by introducing obvious markers in US images and establishing a connection between these markers and image poses.

The paper has twofold contributions: 1) We devised a novel coupling pad for 3D US reconstruction, which can be easily integrated into the traditional 2D US scanning process. The pad features 3 N-shaped lines, providing 3D spatial information without relying on any tracking devices. 2) We developed a coarse-to-fine optimization method for the pose calculation from sequential 2D US images, incorporating a distance-topology discrepancy reduction strategy in the optimization process. To our knowledge, this is the first study to achieve sensorless freehand 3D US based on a simple solid coupling pad.

2 Method

The key idea of our solution is incorporating markers into the US images and linking them to the image poses. To achieve this, we developed a coupling pad made of solid hydrogel, which was fixed in a handhold fixture, as shown in Fig. 1. The coupling pad includes three layers of N-shaped nylon lines. During each scanning session, the pad was affixed to the target object, and sequential US images with obvious markers could be acquired.

Given a sequence of US images $\mathcal{I} = \{I_i \mid i = 1, 2, \ldots, N_I\}$, our objective is to estimate the corresponding pose $\mathcal{G} = \{(t_x, t_y, t_z, \phi_x, \phi_y, \phi_z)_i \mid i = 1, 2, \ldots, N_I\}$ for each frame. Here, $(t_x, t_y, t_z)_i$ corresponds to the components of translation, and $(\phi_x, \phi_y, \phi_z)_i$ represents the Euler angles.

The workflow of our method is depicted in Fig. 2. In the initialization phase, the 2D coordinates of the maker points are calculated. These coordinates, along with the geometry of N-shaped lines, are utilized to estimate the translations of all images. During the optimization phase, the proposed novel distance-topology discrepancy reduction (DTDR) strategy is employed to refine the initial poses. Finally, 3D images are reconstructed through interpolation according to [9]. The details will be discussed in the subsequent sections.

2.1 Initialization

In this step, we assume the image poses exhibit no rotation relative to the world coordinates. Only the translation was estimated, following the principle of similar triangles. The world coordinate system, as shown in Fig. 2, is located at the bottom-left corner of the topmost N-shaped line, with the x, y, and z-axis colored by red, green, and blue, respectively.

For the i^{th} US image, the detected marker points, generated by N_L layers of N-shaped lines are denoted as $\mathcal{P}_i^{det} \in \mathbb{R}^{3N_L \times 2}$. For the j^{th} layer of N-shaped lines, we denote its offset from the first layer as b_j, and define the image point of its middle diagonal line as p_{ij}^m. As shown in Fig. 2, the distances from the

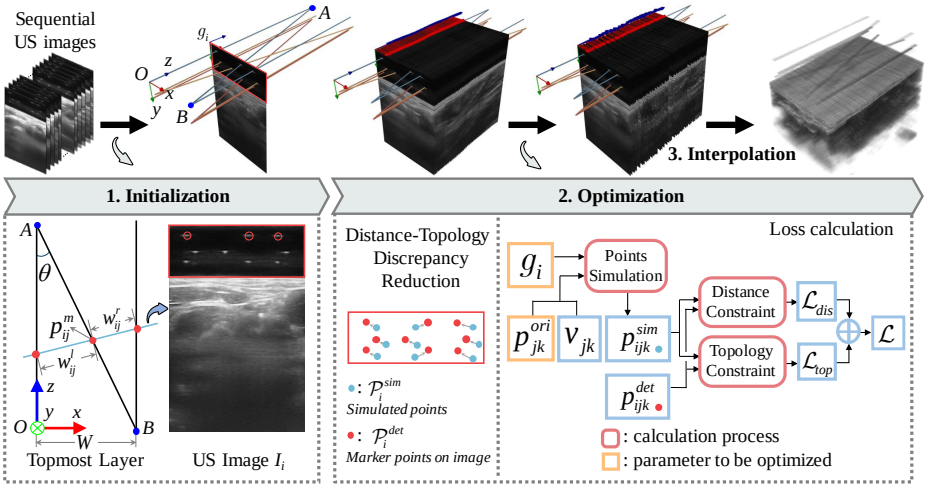

Fig. 2. Overview of our workflow.

midpoint p_{ij}^m to the left and right points on the N-shaped line are labeled as w_{ij}^l and w_{ij}^r, respectively. OB's length is denoted as W. By applying the principle of similar triangles, we can calculate the 3D coordinates of p_{ij}^m and the translation of the image pose. The calculation is expressed as:

$$p_{ij}^m = \left[\frac{w_{ij}^l}{w_{ij}^l + w_{ij}^r} W, 0, \frac{1}{\tan\theta} \frac{w_{ij}^r}{w_{ij}^l + w_{ij}^r} W \right]^\mathsf{T} + b_j, \tag{1}$$

$$(t_x, t_y, t_z)_i = \frac{1}{N_L} \sum_{j=1}^{N_L} p_{ij}^m - r[u_{ij}^m, v_{ij}^m, 0]^\mathsf{T}, \tag{2}$$

where u_{ij}^m, v_{ij}^m denote the pixel coordinates of the middle point in the jth layer of the ith US image, and r represents image spacing. When N-shaped line is flipped, the values of w_{ij}^l and w_{ij}^r are swapped.

2.2 Optimization

In this section, the initial image poses are further optimized. Considering that fabrication errors may cause displacement of the N-shaped lines from their ideal positions, we also optimize the positions of the N-shaped lines to improve pose estimation accuracy. To achieve this, we introduce a loss function defined as:

$$\mathcal{L} = \lambda_{dis}\mathcal{L}_{dis} + \lambda_{top}\mathcal{L}_{top}, \tag{3}$$

where $\mathcal{L}_{top}$ quantifies the topology discrepancy between the simulated points $\mathcal{P}_i^{sim} \in \mathbb{R}^{3N_L \times 2}$ (generated by the N-shaped lines passing through the i^{th} image plane) and the corresponding detected points in the image, $\mathcal{P}_i^{det}$. Meanwhile,

$\mathcal{L}_{dis}$ quantifies the distance discrepancy between corresponding points $\mathcal{P}_i^{sim}$ and $\mathcal{P}_i^{det}$. The weights λ_{dis} and λ_{top} serve to balance the two components of the loss. The loss function is further optimized using gradient descent.

Distance Constraints. We define the points on the N-shaped line as:

$$p_{jk}^{line} = p_{jk}^{ori} + sv_{jk}. \tag{4}$$

Here, p_{jk}^{line} represents a point on the k^{th} line of the N-shaped line in the j^{th} layer. $p_{jk}^{ori} \in \mathbb{R}^3$ and $v_{jk} \in \mathbb{R}^3$ denote the line's origin and direction, with s as a scalar. The indices j and k range from 1 to N_L and 1 to 3, respectively.

The points p_i^{plane} on the plane of the i^{th} US image satisfy the following constraint, where n_i and p_i^{ori} respectively represent the normal vector and the origin of the US image.

$$n_i \cdot (p_i^{plane} - p_i^{ori}) = 0. \tag{5}$$

The k^{th} line of the N-shaped lines in the j^{th} layer intersects with the i^{th} plane at the point p_{ijk}^{plane}, which could be obtained by substituting equation (4) into equation (5) (setting $p_{jk}^{line} = p_i^{plane}$). Specifically, we transform the pose $g_i \in \mathcal{G}$ into a rotation matrix $R_i \in \mathbb{R}^{3\times3}$ and a translation vector $t_i \in \mathbb{R}^3$. Here, $n_i = R_i[:, 3]$ represents the image plane's normal vector, and $p_i^{ori} = t_i$ is the i^{th} plane's origin. The intersection point p_{ijk}^{plane} in the 3D world coordinate system, transformed by the corresponding pose g_i, yields the 2D coordinates $p_{ijk}^{sim} \in \mathcal{P}_i^{sim}$ on the image. Considering the corresponding marker point detected in the image, $p_{ijk}^{det} \in \mathcal{P}_i^{det}$,the loss function is formulated as:

$$\mathcal{L}_{dis} = \frac{1}{3N_I N_L} \sum_{i,j,k} \|p_{ijk}^{sim} - p_{ijk}^{det}\|_2. \tag{6}$$

Topology Constraints. Due to the image noise, optimization based on the distance constraints alone is not sufficiently robust for pose estimation, particularly for rotation. To this end, we incorporate additional topology constraints using the scoring mechanism proposed by Bai et al. [20]. For the i^{th} frame scan:

$$\mathbf{A}_i[m, n] = \left[1 - \frac{(d_{mn}^{sim} - d_{mn}^{det})}{d_{thr}^2}\right]_+, \tag{7}$$

where

$$d_{mn}^{sim} = \|p_m - p_n\|,\ p \in \mathcal{P}_i^{sim}; \quad d_{mn}^{det} = \|\hat{p}_m - \hat{p}_n\|,\ \hat{p} \in \mathcal{P}_i^{det}. \tag{8}$$

Here, $\mathbf{A}_i[m, n]$ measures the discrepancy between the relative distances of points within the simulated $\mathcal{P}_i^{sim}$ and those detected in $\mathcal{P}_i^{det}$ in I_i. m, n denotes the index of points. The parameter d_{thr} dictates the sensitivity to differences in relative distances. The notation $[\cdot]_+ = \max(\cdot, 0)$ ensures non-negativity. A score in

$\mathbf{A}_i$ closer to 1 indicates greater similarity between the pairs of relative distances. The loss function for topology differences can be expressed as:

$$\mathcal{L}_{top} = \frac{1}{N_I}\sum_{i}^{N_I} -\log(\frac{1}{(3N_L)^2}\mathbf{1}^\mathsf{T}\mathbf{A}_i\mathbf{1}). \tag{9}$$

Here, $\mathbf{1}$ represents a column vector of ones. Reducing $\mathcal{L}_{top}$ results in the topology of $\mathcal{P}_i^{sim}$ more closely approximating that of $\mathcal{P}_i^{det}$.

3 Experiments and Results

In our implementation, the parameters for the N-shaped line are as follows: $N_L = 3$, $W = 25.5$, $\theta = 12.41°$, $b_2 = [2.5, 4.8, 0]^\mathsf{T}$, $b_3 = [0, 7.4, 0]^\mathsf{T}$. The optimization parameters are: $d_{thr} = 0.6$; $\lambda_{dis} = 0.1$; $\lambda_{top} = 1$. The unit of distance is consistently adopted as millimeters. Optimization was performed using the Adam optimizer, with a learning rate of 10^{-2}. The generated volume size is $400 \times 600 \times 800$ with a voxel resolution of $0.1 \times 0.1 \times 0.1$ mm. All codes were implemented in PyTorch and run on an RTX 4090 GPU.

Pose Accuracy Estimation. We performed a simulation for the estimation of pose accuracy as previous studies [9,10], where the ground truth of image poses could be obtained. We followed the simulation outlined in [9], and added simulated N-shaped lines to 3D images. Subsequently, synthetic sequential 2D US images with makers were generated from 3D images. Specifically, we generated 100 linear scanning sequences with randomly assigned frame counts (ranging from 80 to 100 frames) and scanning lengths spanning from 65mm to 80mm. To better simulate real-world scanning conditions, Gaussian noise was added to the pose of each frame. Furthermore, the positions of marker points were also perturbed along the horizontal and vertical axes, introducing noise within the ranges of -0.2 to 0.2 mm and -0.1 to 0.1 mm, respectively. By utilizing the generated images as input for the proposed method, we could estimate the image poses and compare them with the ground truth. We evaluated the accuracy of the estimated poses using metrics proposed by [10], including the Final Drift Rate (FDR), Average Drift Rate (ADR), Maximum Drift (MD), Sum of Drift (SD), and Symmetric Hausdorff Distance (HD).

Table 1. The mean(std) FDR and ADR of different methods

Methods	**FDR(%) ↓**	**ADR(%) ↓**
DCL-Net [3]	35.90 (20.35)	37.04 (13.65)
RecON [9]	25.90 (18.33)	30.36 (13.95)
MoNet [7]	12.75 (9.05)	19.05 (11.46)
Ours	**2.74 (2.98)**	**3.35 (3.24)**

Table 2. The mean (std) results of ablation experiments.

$\mathcal{L}_{dis}$	$\mathcal{L}_{top}$	**FDR(%) ↓**	**ADR(%) ↓**	**MD(mm) ↓**	**SD(mm) ↓**	**HD(mm) ↓**
		13.76 (7.51)	15.55(7.16)	10.27(5.52)	463.18(246.47)	10.20(5.55)
✓		11.16(16.39)	13.34(17.16)	9.51(11.88)	3397.22(553.95)	8.38(12.09)
	✓	7.624(4.12)	14.20(4.90)	6.75(2.60)	295.58(123.55)	6.645(2.62)
✓	✓	**2.74(2.98)**	**3.35(3.24)**	**2.52(2.25)**	**100.29(103.02)**	**2.05(2.06)**

Comparisons with state-of-the-art (SOTAs): The results in Table 1 show that our method has a 4.7x lower FDR and a 5.7x lower ADR compared to the SOTA, indicating significant improvements achieved by our method. Previous deep-learning solutions [3,9,7] mainly rely on the analysis of latent image patterns between adjacent US images, resulting in cumulative drift error. In our method, robust spatial information is integrated into the US images through the use of the coupling pad, closely associating the pose of each US image with distinct marker patterns. Consequently, the cumulative drift error is reduced.

Ablation study for the loss function: To examine the impact of $\mathcal{L}_{dis}$ and $\mathcal{L}_{top}$ in the loss function, we conducted ablation experiments and the results are summarized in Table 2. When using either $\mathcal{L}_{dis}$ or $\mathcal{L}_{top}$ as the sole loss function, the optimization performance was reduced, indicated by an increase in all the metric values. Table 2 demonstrates the complementary nature of $\mathcal{L}_{dis}$ and $\mathcal{L}_{top}$.

Reconstruction Accuracy. To evaluate the accuracy and robustness of our method in practical US reconstruction, we scanned and reconstructed two types of phantom: a 9-line phantom and a solid phantom (melamine sponge), as shown in Fig. 3. A portable linear US probe (Frequency 10MHz, SonoStar Technologies, China) was used for scanning, and the pixel spacing of the US images is 0.044 mm. Considering the variability of scanning styles in practice, we evaluated three scanning modes: Linear, Oscillating, and Back-and-forth (see Fig. 4c). The frame counts of different scans range from 80 to 150.

Reconstruction accuracy for the 9-line phantom: For each scanning mode, the 9-line phantom underwent 15 scans. Following the reconstruction of 3D US, 9 lines were extracted from the image (denoted as $\mathcal{S}_{lines}$) and registered to the theoretical lines (denoted as $\mathcal{T}_{lines}$) using Iterative Closest Point (ICP) method, as shown in Fig. 4a. Finally, the reconstruction error could be estimated

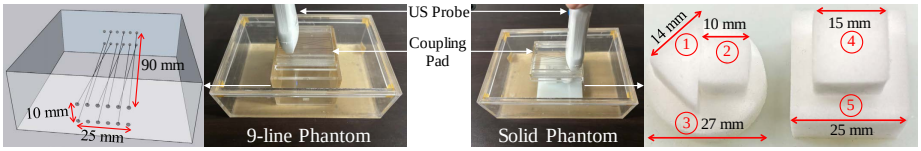

Fig. 3. Reconstruction accuracy experiments. On the left and right are the 9-line phantom and solid phantom, along with the lengths of their key parts.

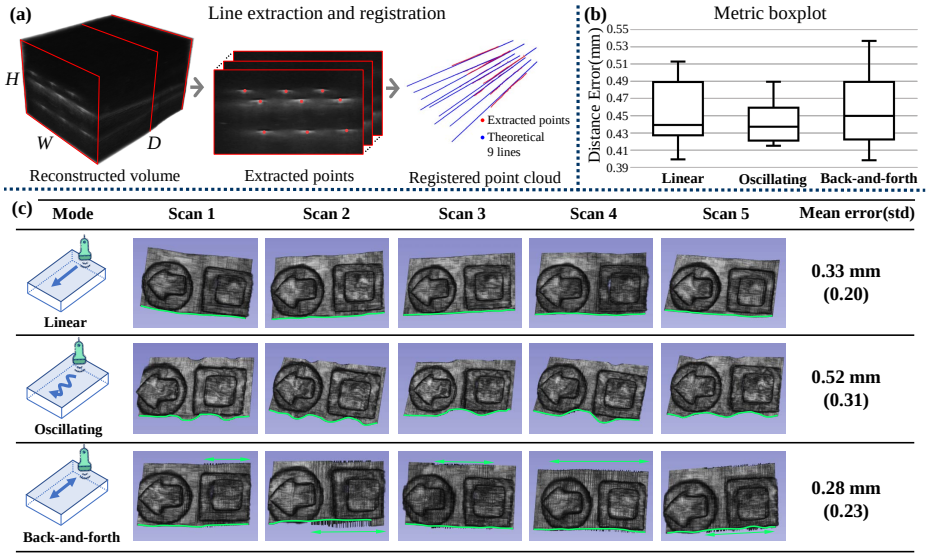

Fig. 4. Phantom reconstruction results. a) Extracting line point clouds from the reconstructed volume of the 9-line phantom. b) The reconstruction errors of the 9-line phantom. c) The reconstruction results and distance error of the solid phantom.

by calculating the mean distance from $\mathcal{S}_{lines}$ to the corresponding $\mathcal{T}_{lines}$. The evaluation results presented in Fig. 4b show that the mean distance errors for most scanning modes fall below 0.5 mm.

Reconstruction accuracy for the solid phantom: The solid phantom was scanned 5 times repeatedly for each scanning mode. For each reconstructed US volume, 5 lengths marked in Fig. 3 were measured and compared with the ground truth. The visualization of the volume and the reconstruction error results are presented in Fig. 4c. It is evident that the reconstructed shape closely approximates the actual phantom shape, displaying mean reconstruction errors ranging from 0.2 to 0.5 mm across various scanning modes. Furthermore, the reconstructed US volumes also depict the probe trajectories, as evidenced by the volume edges. These findings highlight the robustness of our method, indicating a small influence on the reconstruction from scanning styles.

The proposed coupling pad solution for sensorless 3D reconstruction presents several advantages. The low-cost coupling pad can seamlessly adapt to different linear probes, and it can be easily integrated into the conventional 2D scanning process, requiring no specialized skills. However, its current design is primarily for linear probes and may not be suitable for other US probes. Future work will focus on developing a pad designed for convex probes and conducting more in vivo experiments to confirm its effectiveness.

4 Conclusion

In this study, we designed a novel coupling pad for sensorless freehand 3D US reconstruction. The coupling pad is characterized by its three N-shaped lines, enabling the acquisition of 3D spatial information without relying on external tracking devices. Furthermore, we introduced a distance-topology discrepancy reduction strategy to improve the accuracy of pose estimation. Results from both simulated and phantom studies indicate that our approach outperforms SOTAs in terms of performance.

Acknowledgements. This work was supported by the National Natural Science Foundation of China (No. 62201448), Zhejiang Provincial Natural Science Foundation of China (No. LQ23F010022), the China Postdoctoral Science Foundation (No. 2022M712548), and the Key Research and Development Program of Shaanxi Province under Grant. 2021GXLH-Z-097.

Disclosure of Interests. The authors have no competing interests to declare that are relevant to the content of this article.

References

1. Chen, J.-F. et al.: Determination of scan-plane motion using speckle decorrelation: Theoretical considerations and initial test. Int. J. Imaging Syst. Technol. 8, 1, 38–44 (1997). https://doi.org/10.1002/(SICI)1098-1098(1997)8:1<38::AID-IMA5>3.0.CO;2-U
2. El Hadramy, S. et al.: Trackerless Volume Reconstruction from Intraoperative Ultrasound Images. In: Greenspan, H. et al. (eds.) Medical Image Computing and Computer Assisted Intervention – MICCAI 2023. pp. 303–312 Springer Nature Switzerland, Cham (2023). https://doi.org/10.1007/978-3-031-43999-5_29
3. Guo, H. et al.: Sensorless Freehand 3D Ultrasound Reconstruction via Deep Contextual Learning. In: Martel, A.L. et al. (eds.) Medical Image Computing and Computer Assisted Intervention – MICCAI 2020. pp. 463–472 Springer International Publishing, Cham (2020). https://doi.org/10.1007/978-3-030-59716-0_44
4. Guo, H. et al.: Ultrasound Volume Reconstruction From Freehand Scans Without Tracking. IEEE Trans. Biomed. Eng. 70, 3, 970–979 (2023). https://doi.org/10.1109/TBME.2022.3206596
5. Huang, Q., Zeng, Z.: A Review on Real-Time 3D Ultrasound Imaging Technology. BioMed Research International. 2017, 1–20 (2017). https://doi.org/10.1155/2017/6027029
6. Li, Q. et al.: Trackerless Freehand Ultrasound with Sequence Modelling and Auxiliary Transformation Over Past and Future Frames. In: 2023 IEEE 20th International Symposium on Biomedical Imaging (ISBI). pp. 1–5 IEEE, Cartagena, Colombia (2023). https://doi.org/10.1109/ISBI53787.2023.10230773
7. Luo, M. et al.: Deep Motion Network for Freehand 3D Ultrasound Reconstruction. In: Wang, L. et al. (eds.) Medical Image Computing and Computer Assisted Intervention – MICCAI 2022. pp. 290–299 Springer Nature Switzerland, Cham (2022). https://doi.org/10.1007/978-3-031-16440-8_28

8. Luo, M. et al.: Multi-IMU with Online Self-consistency for Freehand 3D Ultrasound Reconstruction. In: Greenspan, H. et al. (eds.) Medical Image Computing and Computer Assisted Intervention – MICCAI 2023. pp. 342–351 Springer Nature Switzerland, Cham (2023). https://doi.org/10.1007/978-3-031-43907-0_33
9. Luo, M. et al.: RecON: Online learning for sensorless freehand 3D ultrasound reconstruction. Medical Image Analysis. 87, 102810 (2023). https://doi.org/10.1016/j.media.2023.102810
10. Luo, M. et al.: Self Context and Shape Prior for Sensorless Freehand 3D Ultrasound Reconstruction. In: De Bruijne, M. et al. (eds.) Medical Image Computing and Computer Assisted Intervention – MICCAI 2021. pp. 201–210 Springer International Publishing, Cham (2021). https://doi.org/10.1007/978-3-030-87231-1_20
11. Miura, K. et al.: Localizing 2D Ultrasound Probe from Ultrasound Image Sequences Using Deep Learning for Volume Reconstruction. In: Hu, Y. et al. (eds.) Medical Ultrasound, and Preterm, Perinatal and Paediatric Image Analysis. pp. 97–105 Springer International Publishing, Cham (2020). https://doi.org/10.1007/978-3-030-60334-2_10
12. Miura, K. et al.: Pose Estimation of 2D Ultrasound Probe from Ultrasound Image Sequences Using CNN and RNN. In: Noble, J.A. et al. (eds.) Simplifying Medical Ultrasound. pp. 96–105 Springer International Publishing, Cham (2021). https://doi.org/10.1007/978-3-030-87583-1_10
13. Morgan, M.R. et al.: Versatile Low-Cost Volumetric 3-D Ultrasound Platform for Existing Clinical 2-D Systems. IEEE Trans. Med. Imaging. 37, 10, 2248–2256 (2018). https://doi.org/10.1109/TMI.2018.2821901
14. Mozaffari, M.H., Lee, W.-S.: Freehand 3-D Ultrasound Imaging: A Systematic Review. Ultrasound in Medicine & Biology. 43, 10, 2099–2124 (2017). https://doi.org/10.1016/j.ultrasmedbio.2017.06.009
15. Ning, G. et al.: Spatial Position Estimation Method for 3D Ultrasound Reconstruction Based on Hybrid Transfomers. In: 2022 IEEE 19th International Symposium on Biomedical Imaging (ISBI). pp. 1–5 IEEE, Kolkata, India (2022). https://doi.org/10.1109/ISBI52829.2022.9761499
16. Prevost, R. et al.: 3D freehand ultrasound without external tracking using deep learning. Medical Image Analysis. 48, 187–202 (2018). https://doi.org/10.1016/j.media.2018.06.003
17. Prevost, R. et al.: Deep Learning for Sensorless 3D Freehand Ultrasound Imaging. In: Descoteaux, M. et al. (eds.) Medical Image Computing and Computer-Assisted Intervention - MICCAI 2017. pp. 628–636 Springer International Publishing, Cham (2017). https://doi.org/10.1007/978-3-319-66185-8_71
18. Tuthill, T.A. et al.: Automated three-dimensional US frame positioning computed from elevational speckle decorrelation. Radiology. 209, 2, 575–582 (1998).https://doi.org/10.1148/radiology.209.2.9807593
19. Xie, Y. et al.: Image-Based 3D Ultrasound Reconstruction with Optical Flow via Pyramid Warping Network. In: 2021 43rd Annual International Conference of the IEEE Engineering in Medicine & Biology Society (EMBC). pp. 3539–3542 IEEE, Mexico (2021). https://doi.org/10.1109/EMBC46164.2021.9630853
20. Bai, X. et al.: PointDSC: Robust point cloud registration using deep spatial consistency. In: Proceedings of the IEEE/CVF Conference on Computer Vision and Pattern Recognition, pp. 15859–15869 (2021) https://doi.org/10.1109/cvpr46437.2021.01560